RSC Advances

PAPER

Published on 20 July 2026
Licensed under CC-BY-NC 4.0

Check for updates

Cite this: DOI: 10.1039/d6ra04385b

Engineering an Ni_9S_8@Fe-NiP-O_2 core–shell catalyst: high activity and stability for oxygen/hydrogen evolution in alkaline and ammonia-containing media

Kangkang Zhao,[a] Haonan Jiang,[a] Yunjie Ke,*[a] Meizhen Dai,[a] Hengqi Liu,[a] Shiwei Song,[a] Yucai Li,[a] Depeng Zhao,[a] Rongda Zhao*[b] and Lihua Miao*[c]

To address the issues of low activity, inadequate stability, and susceptibility to deactivation in ammonia-containing alkaline water electrolysis catalysts, Ni_9S_8@Fe-NiP-O_2 bifunctional electrocatalysts with a fractional core–shell structure were effectively synthesised using a phosphating oxidation coupling strategy. The Ni_9S_8@N_3Fe-PBA precursor underwent structural transformation to form porous cubic-like particles, exhibiting significant electronic interaction between the Ni_9S_8 core and the Fe-NiP-O_2 shell, which effectively modulated the surface electronic structure. Electrochemical assessments indicate that in a 1 M KOH solution, the oxygen evolution reaction (OER) overpotential of Ni_9S_8@Fe-NiP-O_2 is at 235.6 mV at 20 mA cm^{-2}, while the hydrogen evolution reaction (HER) overpotential is as low as 125.4 mV. The Tafel slope and charge transfer resistance are markedly superior to those of $Ni(OH)_2$, Ni_9S_8, and other comparison samples, exhibiting the highest electrochemical double layer capacitance (C_{dl}) and electrochemical active surface area (ECSA). In a 25% ammonia aqueous solution, the catalyst exhibits exceptional catalytic activity for both OER and HER, with superior overpotential, kinetics, and mass transfer characteristics. The comprehensive water electrolysis assessment indicates that Ni_9S_8@Fe-NiP-O_2 demonstrates great efficiency and stability in water electrolysis across alkaline systems, ammonia aqueous solutions, and membrane electrode assemblies (MEAs). The current density in the MEA system can attain 950 mA cm^{-2} at 60 °C. The results show that the core–shell synergistic effect, multi-stage porous structure and multi-component electronic regulation jointly endow the catalyst with excellent bifunctional catalytic activity and ammonia resistance.

Received 20th May 2026
Accepted 12th July 2026

DOI: 10.1039/d6ra04385b

rsc.li/rsc-advances

1 Introduction

The escalating depletion of fossil fuels and the exacerbation of associated issues have rendered clean and reliable energy carriers a paramount worldwide concern. Hydrogen energy is considered a crucial element of the future energy system because of its high energy density, minimal carbon emissions, and diverse sources.[1–5] The electrolysis of water for hydrogen production has emerged as a significant method for large scale hydrogen generation due to its environmentally friendly procedure, high product purity, and seamless integration with renewable energy sources. Water electrolysis encompasses two and a half reactions: the oxygen evolution reaction (OER) and the hydrogen evolution reaction (HER), with kinetics that often necessitate high-efficiency catalysts to overcome reaction energy barriers. Despite the superior catalytic efficacy of precious metal based catalysts, their high cost, limited availability, and inadequate stability hinder their suitability for large scale industrial applications.[6–10] Consequently, cost effective, highly active, and stable non-noble metal bifunctional electrocatalysts have emerged as a significant research focus in the domain of water electrolysis.[11,12]

In recent years, transition metal sulphides, phosphides, and Prussian blue analogues (PBA) have increasingly garnered attention as water electrolysis catalysts due to their tunable electronic structures, abundant active sites, and excellent electrical conductivity.[13–16] Nonetheless, single-component materials encounter numerous challenges in practical applications, including inadequate active site density, suboptimal electrical conductivity, and vulnerability to performance degradation at elevated current densities, particularly in ammonia-containing electrolytes, which are susceptible to rapid inactivation due to toxic effects. To solve the above problems, researchers have proposed effective strategies such as constructing core–shell

[a]School of New Energy, Shenyang Institute of Engineering, Shenyang, Liaoning, CN 110136, P. R. China

[b]School of Materials Science and Engineering, Liaoning University of Technology, Jinzhou 110870, PR China

[c]School of Medical Information Engineering, Shenyang Medical College, Shenyang, Liaoning, 110034, P. R. China. E-mail: miaolihua@symc.edu.cn

© 2026 The Author(s). Published by the Royal Society of Chemistry

hierarchical structures, realizing multicomponent synergistic modification and precisely regulating interfacial electronic structures. These strategies are intended to boost the environmental adaptability, ammonia resistance and structural stability of catalysts toward overall water splitting under alkaline KOH and ammonia solution conditions.[17,18] They can optimize the adsorption and desorption behaviors of reaction intermediates, accelerate charge transfer kinetics, and further strengthen the structural stability of as-prepared catalysts. Utilising Ni_9S_8@N_3Fe-PBA as the precursor, this study effectively synthesised a bifunctional electrocatalyst, Ni_9S_8@Fe-NiP-O_2, featuring a hierarchical core–shell architecture by a combined phosphating–oxidation heat-treatment approach. The crystal structure, surface chemical state, and micromorphology of the material were meticulously characterised, and its electrocatalytic performance for the oxygen evolution reaction (OER) and hydrogen evolution reaction (HER) in alkaline solutions and ammonia-containing systems was thoroughly examined. Additionally, tests for overall water splitting using a two-electrode system and the performance of the membrane electrode assembly (MEA) were conducted. The mechanisms by which the core–shell structure, hierarchical porous morphology, and intercomponent electronic interactions affect catalytic activity, reaction kinetics, and charge-transfer behaviour were thoroughly examined. The catalyst's structural stability and performance benefits in ammonia-rich conditions were elucidated. The research findings offer empirical data and theoretical backing for the development of high-efficiency, ammonia-resistant non-noble metal electrocatalysts for water electrolysis.

2 Experimental results and discussion

2.1 Structural characterization of materials

The XRD characteristics of Ni_9S_8@N_3Fe-PBA and Ni_9S_8@Fe-NiP-O_2 samples are presented in Fig. 1a. For Ni_9S_8@N_3Fe-PBA, three well-defined diffraction peaks centered at 25.24°, 31.36° and 35.88° are identified, which correspond to the (220) plane of $K_2FeNi(CN)_6$, and the (222) and (312) planes of Ni_9S_8, respectively. These results are in good agreement with the standard PDF card of $K_2FeNi(CN)_6$ (PDF #20-0915) and Ni_9S_8 (PDF #22-1193).In addition, distinct diffraction peaks at 25.2°, 31.4° and 35.9° in the XRD pattern of Ni_9S_8@Fe-NiP-O_2 are assigned to the (220) plane of $K_2FeNi(CN)_6$, the (222) plane of Ni_9S_8 and the (208) plane of Ni_8P_3, which match the standard PDF card of Ni_9P_3 (PDF #65-5516). The XRD results of Ni_9S_8@Fe-NiP-O_2 are also consistent with the corresponding standard PDF cards.

The XRD data collectively validate the effective synthesis of Ni_9S_8@N_3Fe-PBA and Ni_9S_8@Fe-NiP-O_2. X-ray photoelectron spectroscopy (XPS) was conducted to elucidate the elemental composition and chemical valence state of the material's surface.[19] In Ni_9S_8@N_3Fe-PBA (Fig. 1b), distinct peaks corresponding to Ni 2p, Fe 2p, N 1s, O 1s, and C 1s were prominently detected, validating the effective synthesis of Ni_9S_8@N_3Fe-PBA composites with the anticipated elemental composition. After phosphating treatment, the synthesized Ni_9S_8@Fe-NiP-O_2 composite maintains the characteristic XPS signals of Ni 2p, Fe 2p, O 1s, C 1s, and S 2p. Among these signals, the S 2p peak is derived from the inherent Ni_9S_8 phase of the Ni_9S_8@N_3Fe-PBA precursor. In particular, a distinct P 2p peak newly emerges after phosphating, whereas the N 1s signal disappears completely. These results verify the successful phosphating modification of the precursor, the stable preservation of the Ni_9S_8 sulfide phase during the fabrication process, and the effective transformation of the PBA precursor into Fe-NiP-O_2 phosphide-oxide composites. Collectively, these findings strongly demonstrate the successful synthesis of well-defined Ni_9S_8@Fe-NiP-O_2 heterostructured composites.

The P 2p spectrum in Fig. 1c reveals that the phosphated sample displays a distinctive P–M peak at 132.58 eV, where M = Ni/Fe, thereby verifying the effective synthesis of the Ni_8P_3/FeP metal phosphide phase. The peak at 133.78 eV corresponds to the P–Ni/Fe link in the phosphide-oxide intermediate state, signifying a robust electronic interaction between P and Ni/Fe, which is advantageous for modulating the electronic structure and enhancing charge transfer during electrocatalysis. The signal at 134.98 eV is ascribed to P–O species generated by surface oxidation. Fig. 1d illustrates that prior to phosphating, the C 1s spectrum can be deconvoluted into the C=C/C–C peak at 284.8 eV, the C–N peak at 285.28 eV, and the C≡N peak at 288.68 eV. Following phosphating, the C≡N peak vanishes, while the C=C/C–C peak at 284.8 eV persists, and a new C–O/C=O peak emerges at 287.98 eV, signifying the structural alteration of the PBA precursor during phosphating. All binding energies were calibrated use the C 1s peak of adventitious carbon at 284.8 eV.

The analysis of the O 1s spectra in Fig. 1e indicates that the peaks at 531.08 eV and 533.08 eV prior to phosphating correspond to lattice oxygen from Ni–O/Fe–O links in PBA and adsorbed oxygen species, including surface hydroxyl groups and adsorbed water, respectively.[20] Following phosphating, two prominent peaks emerge at 530.88 eV, corresponding to surface hydroxyl oxygen, and at 531.36 eV, ascribed to lattice oxygen in the Fe-NiP-O_2 phosphide-oxide phase. This verifies the successful integration of oxygen into the phosphide-oxide structure, and the existence of surface hydroxyl groups enhances electrocatalytic performance. The N 1s spectrum in Fig. 1f demonstrates that prior to phosphating, the peak at 397.87 eV is attributed to the cyano group (C≡N) in PBA, while the peaks at 399.36 eV and 401.78 eV are associated with pyridinic N and graphitic N, indicating the presence of nitrogen-containing functional groups and carbon substrates. Following phosphating, the C≡N peak vanishes, but new peaks arise at 397.38 eV for metal–N or residual C≡N, 398.38 eV for pyrrolic N, 399.88 eV for pyridinic N, and 400.88 eV for graphitic N. These differences further confirm the structural transition from the PBA precursor to the Fe–NiP–O_2 phosphide-oxide phase.

The Fe 2p spectra in Fig. 1g reveals that both samples display doublet peaks of Fe $2p_{3/2}$ at roughly 711 eV and Fe $2p_{1/2}$ at around 724 eV, along with a Fe^{3+} satellite peak near 718 eV. Following phosphating, the binding energies of Fe 2p exhibit a minor negative shift, signifying robust electronic interactions among Fe, Ni, P, and O atoms, which modulate the valence state

© 2026 The Author(s). Published by the Royal Society of Chemistry

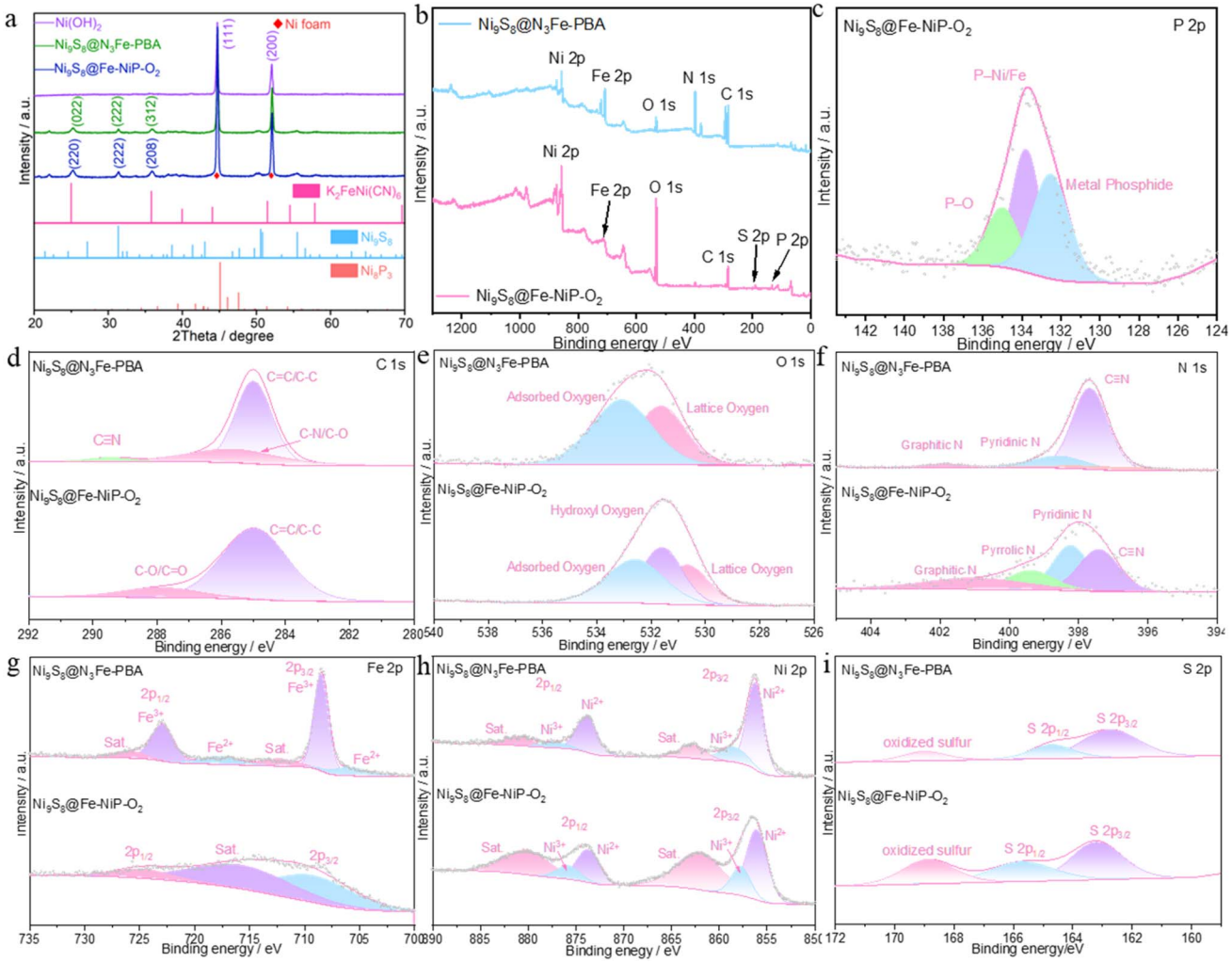


Fig. 1 Structural characterization of the prepared samples (a) XRD patterns of $Ni(OH)_2$, Ni_9S_8@N_3Fe-PBA and Ni_9S_8@Fe-NiP-O_2 (b) survey XPS spectrum (c) XPS spectrum of P 2p (d) C 1s (e) O 1s (f) N 1s (g) Fe 2p (h) Ni 2p (i) S 2p.

of Fe and thus enhance the electrocatalytic efficiency. The Ni 2p spectrum in Fig. 1h indicates that prior to phosphating, Ni^{2+} is observed at 856.38 eV and 873.98 eV, while Ni^{3+} is found at 858.88 eV and 877.28 eV. Following phosphating, the binding energies of Ni 2p exhibit a minor negative change, indicating robust electronic interactions among Ni, P, and O, which alter the valence state of Ni and improve catalytic efficacy. The persistence of satellite peaks verifies the simultaneous presence of Ni^{2+} and Ni^{3+}.The S 2p spectra in Fig. 1i reveals distinctive doublets corresponding to S^{2-} in Ni_9S_8, detected both prior to and following phosphating: S $2p_{3/2}$ at roughly 162.5 eV and S $2p_{1/2}$ at around 163.7 eV, confirming the stability of the Ni_9S_8 phase during phosphating. The intensity of the oxidised sulphur peak at around 169.0 eV escalates post-phosphating, signifying partial oxidation of surface sulphur, which enhances electrocatalytic activity.[21]

Fig. S1a–g illustrate the morphological evolution of the materials as shown by scanning electron microscopy (SEM) pictures. The Ni_9S_8@N_3Fe-PBA precursor exhibits a homogeneous hierarchical nanosheet array structure, characterised by smooth layered nanosheets that are vertically orientated on the substrate, resulting in an extensive specific surface area.[22] Following phosphating, the Ni_9S_8@Fe-NiP-O_2 composite maintains its array structure, while the nanosheets convert into compact and uniform cube-like nanoparticles characterised by a rough and porous surface.[23,24] This structural transformation validates the effective synthesis of the Ni_9S_8@Fe-NiP-O_2 composite, which provides numerous active sites and superior mass transport conditions for electrocatalytic processes. High-magnification SEM of $Ni(OH)_2$ reveals vertically grown smooth ultrathin nanosheets with open interlayer gaps for electrolyte penetration. After sulfurization, Ni_9S_8 inherits the nanosheet scaffold, whose surface is uniformly covered by nanoparticles to form a rough hierarchical structure with enlarged specific surface area and abundant active sites. Low-magnification SEM of Ni_9S_8 displays uniform cross-linked vertical nanosheet arrays over a large area, and the interconnected voids buffer volume variation and accelerate ion transport. Ni_9S_8@NiFe-PBA maintains the original array framework, with dense cubic PBA nanoparticles evenly grown on the nanosheet substrate.

© 2026 The Author(s). Published by the Royal Society of Chemistry

As presented in Fig. S6(a and b), the representative HRTEM images provide clear visual proof of the core–shell structure. In the right image (10 nm scale bar), the particle exhibits a distinct two-tiered contrast profile: the central region shows darker contrast with clear lattice fringes, corresponding to the crystalline Ni_9S_8 core.The surrounding area shows a continuous, uniform, lighter-contrast layer that completely encapsulates the core, corresponding to the Fe-NiP-O_2 shell. A sharp and continuous interface between the core and shell phases is clearly visible. The left image (20 nm scale bar) further confirms this structure, showing the same contrast distribution across multiple particles, with crystalline cores surrounded by uniform outer layers.

2.2 Oxygen evolution performance in alkaline solution

A series of HER and OER experiments were conducted utilising a three-electrode device to examine the electrocatalytic performance of these materials at varying pH values.

Fig. 2 illustrates the electrocatalytic oxygen evolution performance of the samples assessed in a 1 M KOH solution. Fig. 2a illustrates the LSV curves of the five synthesised materials. At a current density of 20 mA cm^{-2}, the overpotential of Ni_9S_8@Fe-NiP-O_2 is 235.6 mV, whereas the overpotentials for $Ni(OH)_2$, Ni_9S_8, Ni_9S_8@N_3Fe-PBA, and Ni_9S_8@N_3FeNiP are 389.6 mV, 264.6 mV, 255.6 mV, and 275.6 mV, respectively. Consequently, Ni_9S_8@Fe-NiP-O_2 demonstrates the minimal overpotential, signifying enhanced oxygen evolution activity relative to the other materials. The overpotential of Ni_9S_8@Fe-NiP-O_2 is 264.6 mV at 40 mA cm^{-2} and 287.6 mV at 60 mA cm^{-2}, consistently outperforming the reference samples across all current densities. This indicates that the composite alteration of Fe-NiP-O_2 with Ni_9S_8 markedly enhances OER catalytic activity, greatly decreases the reaction overpotential, and thus improves oxygen evolution catalytic performance. Fig. 2c illustrates the electrochemical double-layer capacitance (C_{dl}) values of the materials. The C_{dl} values for $Ni(OH)_2$, Ni_9S_8, Ni_9S_8@N_3Fe-PBA, Ni_9S_8@N_3FeNiP, and Ni_9S_8@Fe-NiP-O_2 are 0.00216, 0.10016, 0.04528, 0.03205, and 0.828 mF cm^{-2}, respectively. In comparison, Ni_9S_8@Fe-NiP-O_2 exhibits superior electrocatalytic performance.

Fig. 2d illustrates that the Tafel slope of Ni_9S_8@Fe-NiP-O_2 is 85.3 mV dec^{-1}, whereas the Tafel slopes for the other four materials are 153.4 mV dec^{-1} for $Ni(OH)_2$, 123.8 mV dec^{-1} for Ni_9S_8, 93.8 mV dec^{-1} for Ni_9S_8@N_3Fe-PBA, and 107 mV dec^{-1} for Ni_9S_8@N_3FeNiP. The Tafel slope of Ni_9S_8@Fe-NiP-O_2 is significantly lower than that of its counterparts, signifying the most rapid kinetics of the oxygen evolution reaction, the minimal reaction energy barrier, and the highest intrinsic catalytic activity. Fig. 2e illustrates the Nyquist plots of the synthesised samples. Ni_9S_8@Fe-NiP-O_2 possesses the smallest ionic radius, indicating the lowest charge transfer resistance and the highest ion diffusion rate, hence facilitating a reduction in the OER overpotential. Fig. 2f illustrates the Bode plots of Ni_9S_8@Fe-NiP-O_2, indicating a decline in the phase angle as the potential rises from 0.444 V to 0.558 V. This phenomenon demonstrates expedited electron transfer, which is advantageous for electrocatalytic activities. Fig. S2 depicts that cyclic voltammetry (CV) curves were obtained at different scan rates

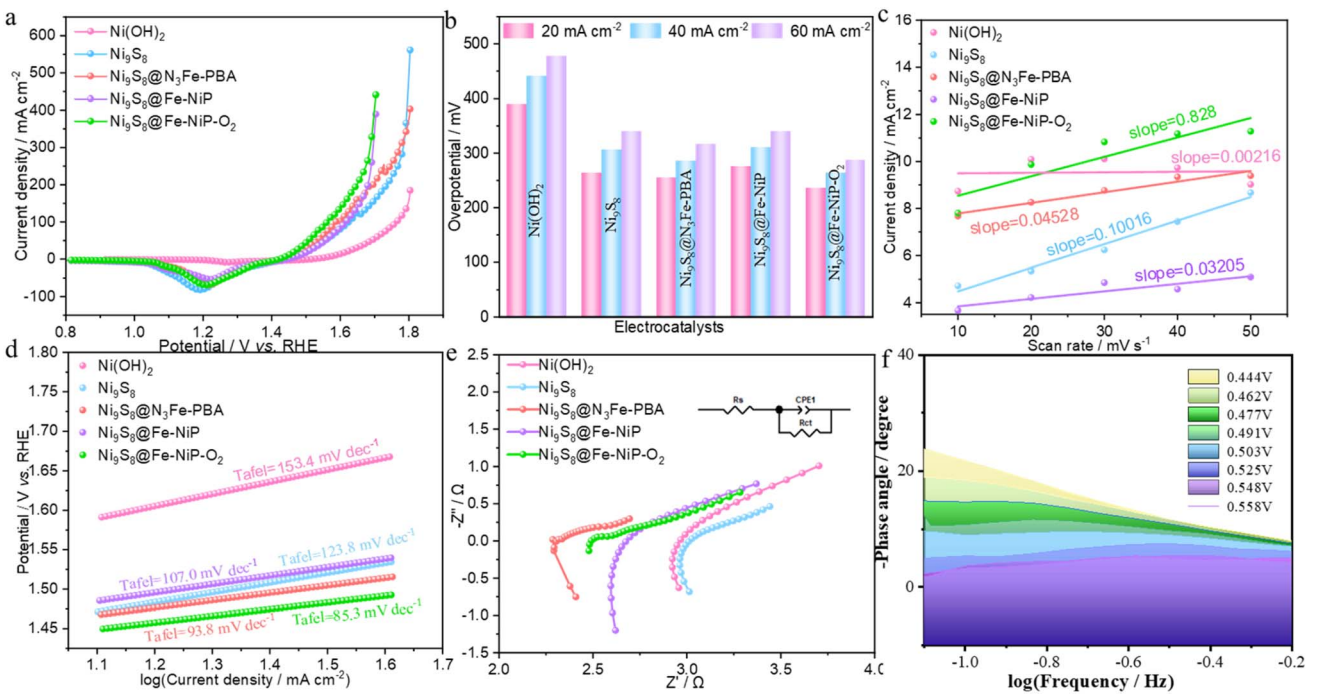


Fig. 2 OER performances of the as-prepared samples (a) LSV curves in 1.0 M KOH solution (b) overpotentials of the material at current densities of 20 mA cm^{-2}, 40 mA cm^{-2} and 60 mA cm^{-2} (c) CV curves of double-layer capacitance (d) Tafel plots (e) Nyquist curves (f) the Bode plots of Ni_9S_8@Fe-NiP-O_2.

© 2026 The Author(s). Published by the Royal Society of Chemistry

(10–50 mV s^{-1}) within the non-faradaic potential range to determine the double-layer capacitance (C_{dl}). All samples demonstrate a linear correlation between current and scan rate, confirming standard double-layer charging behaviour.[25] The Ni_9S_8@Fe-NiP-O_2 catalyst has the highest C_{dl} value, indicating the greatest electrochemical active surface area (ECSA), hence offering numerous exposed active sites for the oxygen evolution reaction (OER).

2.3 Hydrogen evolution performance in alkaline solution

Fig. 3 illustrates the electrocatalytic hydrogen evolution performance of the samples assessed in a 1 M KOH solution. The HER curves in Fig. 3a and b indicate that the Ni_9S_8@Fe-NiP-O_2 material demonstrates a reduced overpotential, particularly at elevated current densities. The overpotential of Ni_9S_8@Fe-NiP-O_2 is 125.4 mV, which is lower than the values of 231.4 mV, 205 mV, 188 mV, and 179.4 mV for $Ni(OH)_2$, Ni_9S_8, Ni_9S_8@N_3Fe-PBA, and Ni_9S_8@N_3FeNiP, respectively. At a current density of −60 mA cm^{-2}, the overpotential of Ni_9S_8@Fe-NiP-O_2 is 213.4 mV, which is lower than the values of 342.4 mV, 310.4 mV, 282.4 mV, and 262.4 mV observed for $Ni(OH)_2$, Ni_9S_8, Ni_9S_8@-N_3Fe-PBA, and Ni_9S_8@N_3FeNiP, respectively. Fig. 3c illustrates that the Tafel slope is a crucial metric for assessing the kinetics of alkaline hydrogen evolution reaction (HER), with a reduced Tafel slope signifying enhanced HER kinetics. The Tafel slope of Ni_9S_8@Fe-NiP-O_2 is 91.79 mV dec^{-1}, marginally lower than 175.13 mV dec^{-1} for $Ni(OH)_2$, 119.75 mV dec^{-1} for Ni_9S_8@N_3Fe-PBA, 126.39 mV dec^{-1} for Ni_9S_8@FeNiP and 152.55 mV dec^{-1} for Ni_9S_8. The advantageous Tafel slope grants Ni_9S_8@Fe-NiP-O_2 exceptional kinetics for the alkaline hydrogen evolution reaction.[26,27]

Fig. 3d illustrates that the electrochemical double-layer capacitance (C_{dl}) values for $Ni(OH)_2$, Ni_9S_8, Ni_9S_8@N_3Fe-PBA, Ni_9S_8@N_3FeNiP, and Ni_9S_8@Fe-NiP-O_2 are 0.00104, 0.01084, 0.01304, 0.00589, and 0.01602 mF cm^{-2}, respectively. In comparison, Ni_9S_8@Fe-NiP-O_2 has superior electrocatalytic performance. The Nyquist plots (Fig. 3e) demonstrate that the Ni_9S_8@Fe-NiP-O_2 catalyst exhibits the smallest semicircle diameter of all samples, signifying the lowest charge-transfer resistance and the most effective charge transport capability at the electrode–electrolyte interface. The diminished R_{ct} value of Ni_9S_8@Fe-NiP-O_2, in contrast to $Ni(OH)_2$, Ni_9S_8, Ni_9S_8@N_3Fe-PBA, and Ni_9S_8@N_3FeNiP, indicates that the incorporation of the Fe-NiP-O_2 phase and the synergistic interaction between Ni_9S_8 and Fe-NiP-O_2 effectively modulate the electronic structure, enhance the electron transfer rate, and consequently optimise the kinetics of the oxygen evolution reaction (OER).[28]

To intuitively assess the comprehensive electrocatalytic performance of the synthesised catalysts for total water splitting, a radar map was created based on six critical parameters: overpotentials and Tafel slopes for both the oxygen evolution reaction (OER) and hydrogen evolution reaction (HER), together with the capacitance values (C_{dl}) for OER and HER. Fig. 3f illustrates that the Ni_9S_8@Fe-NiP-O_2 catalyst possesses the greatest enclosed area and the most saturated curve compared to all other samples. For both OER and HER, it attains the minimal overpotentials and the smallest Tafel slopes, signifying the most rapid reaction kinetics and the highest intrinsic activity. Simultaneously, it exhibits the biggest C_{dl} values,

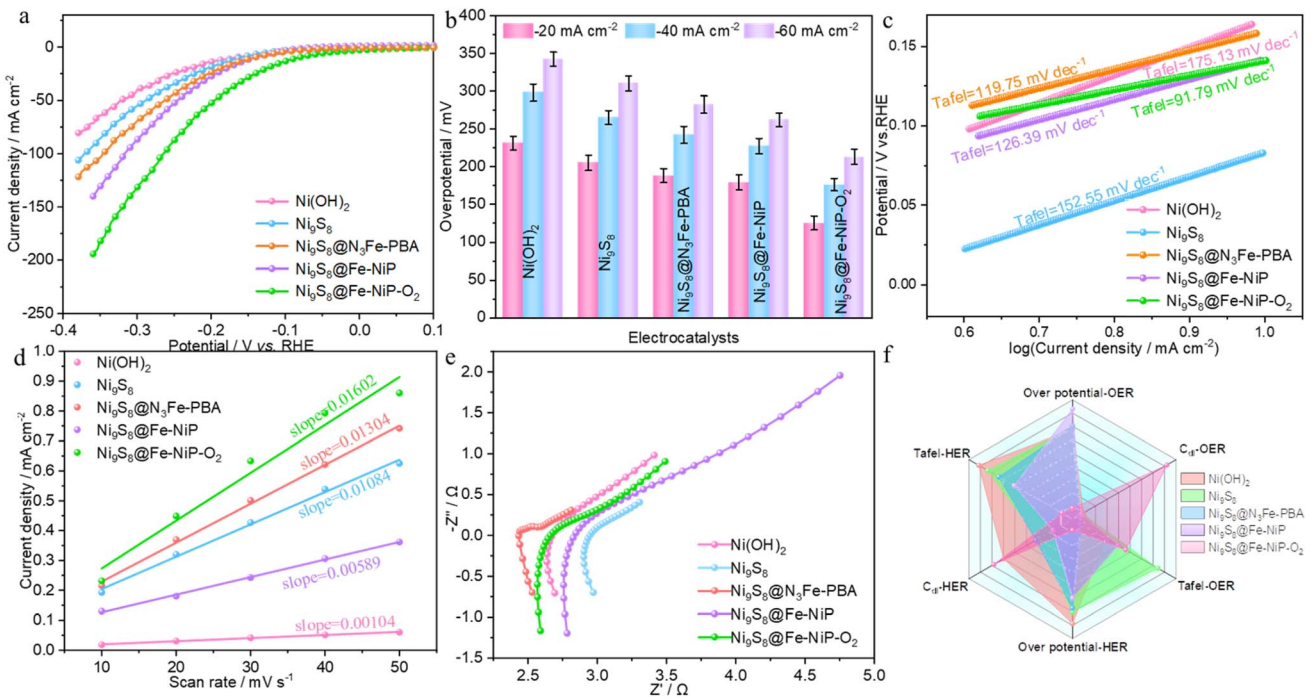


Fig. 3 HER performances of the as-prepared samples (a) LSV curves in 1.0 M KOH solution (b) overpotentials of the material at current densities of −20 mA cm^{-2}, −40 mA cm^{-2} and −60 mA cm^{-2} (c) Tafel plots (d) CV curves of double-layer capacitance (e) Nyquist curves (f) Radar chart.

© 2026 The Author(s). Published by the Royal Society of Chemistry

indicative of the highest electrochemically active surface area and the most accessible active sites. Conversely, the $Ni(OH)_2$ sample exhibits the least enclosed area across all metrics. Ni_9S_8, Ni_9S_8@N_3Fe-PBA, and Ni_9S_8@N_3FeNiP demonstrate progressively enhanced performance with PBA modification and phosphating; nonetheless, they remain inferior to Ni_9S_8@Fe-NiP-O_2. The results unequivocally demonstrate that the fabrication of the hierarchical structured Ni_9S_8@Fe-NiP-O_2 composite significantly improves bifunctional electrocatalytic activity for both OER and HER, resulting in superior overall water splitting performance. The C_{dl} values of the catalysts were ascertained using CV testing at different scan rates in the non-faradaic region (Fig. S3). All samples exhibit quasi-rectangular cyclic voltammetry curves, with current increasing linearly in relation to the scan rate. At an identical scan rate, the Ni_9S_8@Fe-NiP-O_2 catalyst exhibits the greatest current density, correlating with the highest C_{dl} and ECSA. This outcome confirms its extensive active surface area and numerous active sites, which enhance electrocatalytic activity.

2.4 Oxygen evolution performance in ammonia solution

The OER electrocatalytic activity of the synthesised catalysts was assessed *via* linear sweep voltammetry (LSV) in a 25% ammonia solution, as illustrated in Fig. 4a. The Ni_9S_8@Fe-NiP-O_2 catalyst exhibited the highest current density at an equivalent potential, demonstrating outstanding OER activity. At a current density of 20 mA cm^{-2}(Fig. 4b), its overpotential was 308 mV, significantly lower than that of $Ni(OH)_2$ (482.6 mV), Ni_9S_8 (464.6 mV), Ni_9S_8@N_3Fe-PBA (391 mV), and Ni_9S_8@N_3FeNiP (408.6 mV). Notably, Ni_9S_8@Fe-NiP-O_2 maintained the lowest overpotential even at current densities as high as 40 and 60 mA cm^{-2}, indicating excellent catalytic performance under extreme conditions.[29] This outcome verifies that the formation of the Fe-NiP-O_2 shell on the Ni_9S_8 core significantly improves the OER performance.

Tafel plots were generated using the LSV curves to further examine the reaction kinetics of the OER process (Fig. 4d). The Tafel slope of Ni_9S_8@Fe-NiP-O_2 is 48.29 mV dec^{-1}, significantly lower than that of $Ni(OH)_2$ at 69.04 mV dec^{-1}, Ni_9S_8 at 55.89 mV dec^{-1},Ni_9S_8@FeNiP-PBA at 55.4 mV dec^{-1} and Ni_9S_8@FeNiP at 55.17 mV dec^{-1}. The Tafel slope indicates that the OER process demonstrates accelerated reaction kinetics and a reduced energy barrier, affirming that Ni_9S_8@Fe-NiP-O_2 has the highest intrinsic catalytic activity. The electrochemical double-layer capacitance (C_{dl}) was assessed *via* cyclic voltammetry (CV) at different scan speeds inside the non-faradaic potential area, as illustrated in the CV curves of Fig. 4c and S4. All samples display quasi-rectangular cyclic voltammetry curves devoid of discernible redox peaks, signifying that the observed current solely arises from the double-layer charging and discharging mechanism. The C_{dl} value, characterised as the slope of the fitted line of average current against scan rate, is maximised for Ni_9S_8@Fe-NiP-O_2, indicating the maximum electrochemical active surface area (ECSA). The augmented ECSA offers numerous exposed active sites, facilitating the adsorption and desorption of reaction intermediates and enhancing electrocatalytic efficiency.

The interfacial charge transfer characteristics of the catalysts were examined using electrochemical impedance spectroscopy

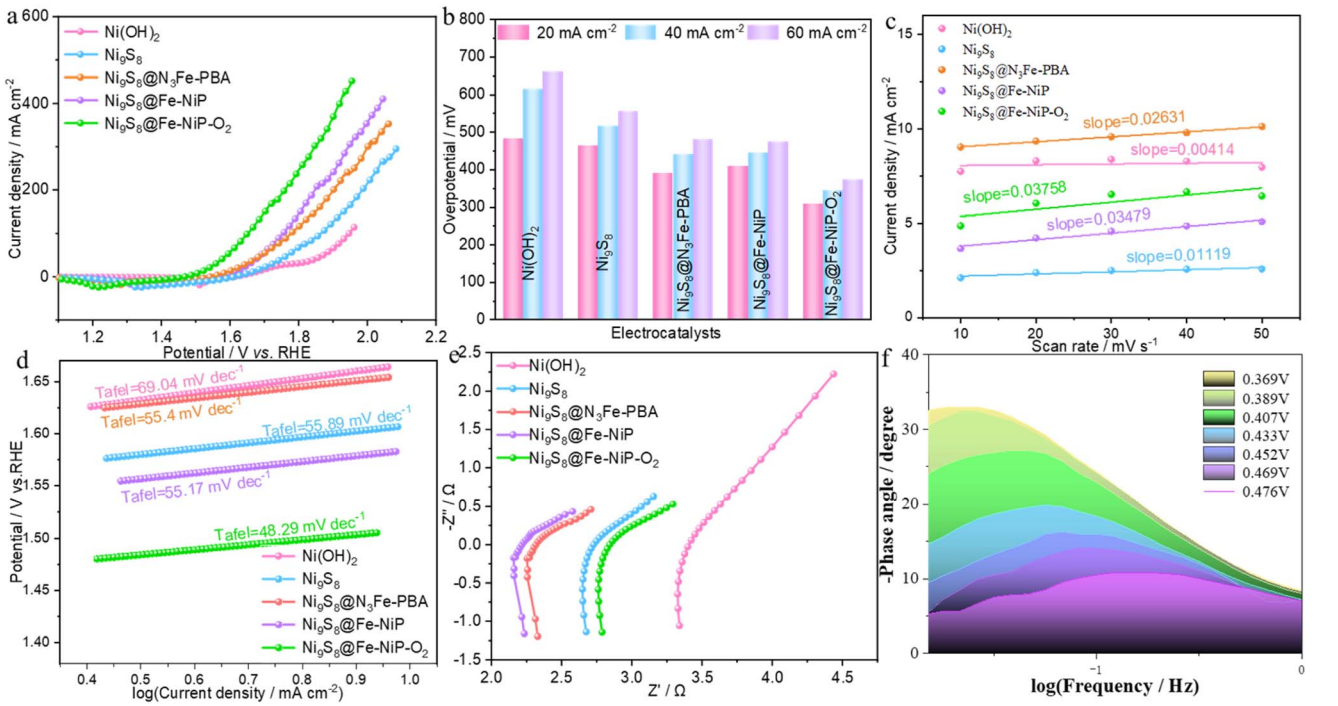


Fig. 4 OER performances of the as-prepared samples (a) LSV curves in a 25% ammonia solution (b) overpotentials of the material at current densities of 20 mA cm^{-2}, 40 mA cm^{-2} and 60 mA cm^{-2} (c) CV curves of double-layer capacitance (d) Tafel plots (e) Nyquist curves (f) the Bode plots of Ni_9S_8@Fe-NiP-O_2.

© 2026 The Author(s). Published by the Royal Society of Chemistry

(EIS) and Bode phase graphs. Fig. 4e illustrates that the Nyquist plot of Ni_9S_8@Fe-NiP-O_2 exhibits the smallest semicircle diameter, signifying the minimal charge transfer resistance (R_{ct}).The fitted R_s values are 2.912, 2.843, 2.715, 2.562,and 2.391 Ω, and the fitted R_{ct} values are 55.27, 47.31, 49.84, 53.62, and 43.95 Ω (see Table S2). In particular, Ni_9S_8@Fe-NiP-O_2 displays the lowest R_{ct} value, indicating the smallest charge transfer barrier and the fastest interfacial electron transfer kinetics for this optimal sample. Furthermore, the CPE parameters elucidate the structural characteristics of the electrode surface. Ni_9S_8@Fe-NiP-O_2 achieves the highest CPE value among all samples, signifying the most ideal capacitive behavior and the most uniform electrode–electrolyte interface. Consistently, Ni_9S_8@Fe-NiP-O_2 shows the narrowest semicircle in the high-frequency region.

The Bode phase graphs (Fig. 4f) further validate that Ni_9S_8@Fe-NiP-O_2 displays the highest phase angle at the OER working potential, indicating that the interface is characterised by resistive behaviour coupled with rapid charge transfer kinetics. The results align with those from LSV and Tafel studies, confirming that Ni_9S_8@Fe-NiP-O_2 exhibits superior charge transfer capabilities and rapid OER reaction kinetics.

2.5 Hydrogen evolution performance in ammonia solution

Fig. 5a illustrates the evaluation of the hydrogen evolution reaction (HER) electrocatalytic activity of the catalysts *via* linear sweep voltammetry (LSV) in a 25% ammonia solution. The Ni_9S_8@Fe-NiP-O_2 catalyst has the largest current density at an equivalent potential, signifying superior hydrogen evolution reaction activity. At −20, −40, and −60 mA cm^{-2}(Fig. 5b), the overpotential of Ni_9S_8@Fe-NiP-O_2 is markedly inferior than that of $Ni(OH)_2$, Ni_9S_8, Ni_9S_8@N_3Fe-PBA, and Ni_9S_8@N_3FeNiP. Even at elevated current densities, Ni_9S_8@Fe-NiP-O_2 exhibits the lowest overpotential, confirming its exceptional HER activity in extreme circumstances.[30] This outcome verifies that the formation of the Fe-NiP-O_2 shell on the Ni_9S_8 core significantly enhances the hydrogen evolution reaction performance in ammonia solution.

Tafel plots were generated using the LSV curves to examine the kinetics of the HER response (Fig. 5d). The Tafel slope of Ni_9S_8@Fe-NiP-O_2 is as low as 121.88 mV dec^{-1}, much lower than those of $Ni(OH)_2$ (173.07 mV dec^{-1}), Ni_9S_8 (152.27 mV dec^{-1}), Ni_9S_8@N_3Fe-PBA (183.76 mV dec^{-1}), and Ni_9S_8@FeNiP (149.21 mV dec^{-1}). The Tafel slope indicates an accelerated reaction rate and reduced energy barrier for the HER process, affirming that Ni_9S_8@Fe-NiP-O_2 exhibits the most advantageous reaction pathway and the highest intrinsic HER activity in ammonia solution.

The electrochemical double-layer capacitance (C_{dl}) was assessed *via* cyclic voltammetry (CV) at different scan rates (10–50 mV s^{-1}) inside the non-faradaic potential region, as illustrated in Fig. 5c and the supplemental CV curves. All samples exhibit quasi-rectangular cyclic voltammetry curves devoid of discernible redox peaks, signifying that the observed current is solely attributable to the double-layer charging and discharging mechanism. The C_{dl} value (slope of the fitted line of average current *versus* scan rate) for Ni_9S_8@Fe-NiP-O_2 is markedly greater than that of other reference samples, indicating a larger electrochemical active surface area (ECSA). The expanded ECSA offers numerous accessible active sites, facilitating the

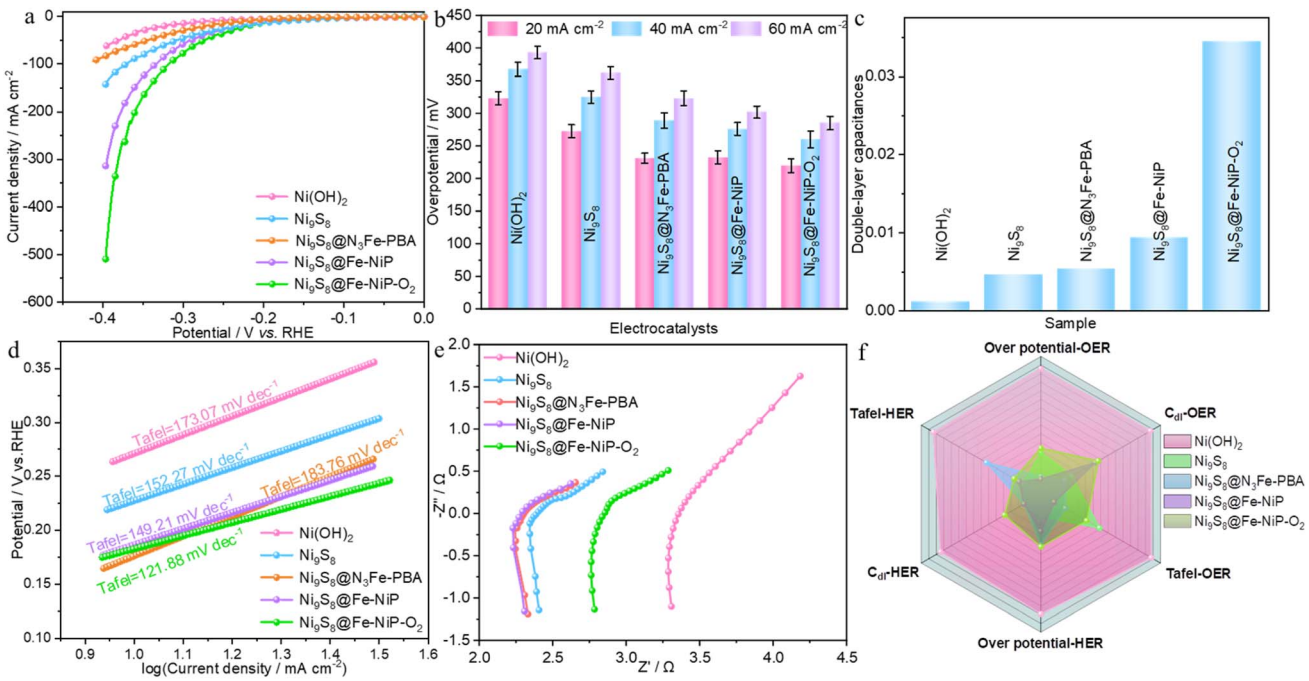


Fig. 5 HER performances of the as-prepared samples (a) LSV curves in a 25% ammonia solution (b) overpotentials of the material at current densities of −20 mA cm^{-2}, −40 mA cm^{-2} and −60 mA cm^{-2} (c) contrast histogram of electric double layer capacitance (d) Tafel plots (e) Nyquist curves (f) Radar chart.

© 2026 The Author(s). Published by the Royal Society of Chemistry

adsorption and desorption of hydrogen intermediates and enhancing HER kinetics.

Electrochemical impedance spectroscopy (EIS) was utilised to investigate the interfacial charge transfer characteristics of the catalysts. Fig. 5e illustrates that the Nyquist plot of Ni_9S_8@Fe-NiP-O_2 exhibits the smallest semicircle diameter, signifying the minimal charge transfer resistance (R_{ct}). This finding verifies that Ni_9S_8@Fe-NiP-O_2 demonstrates the highest efficacy in charge transfer at the electrode–electrolyte interface, aligning with the LSV and Tafel results. The diminished R_{ct} value is ascribed to the synergistic interaction between Ni_9S_8 and Fe-NiP-O_2, which alters the electronic structure and enhances the electron transfer rate.

A radar chart (Fig. 5f) offers a detailed comparison of the HER performance of all samples based on critical parameters such as overpotential, Tafel slope, and C_{dl}. The Ni_9S_8@Fe-NiP-O_2 catalyst demonstrates the most balanced and exceptional performance, characterised by the lowest overpotential, minimal Tafel slope, and optimal C_{dl} value, confirming its remarkable HER activity. The radar chart illustrates that the hierarchical core–shell architecture of Ni_9S_8@Fe-NiP-O_2 significantly improves bifunctional electrocatalytic activity for both OER and HER in ammonia solution.

2.6 Overall water splitting performance of samples in different solutions

The comprehensive water splitting efficacy in a 1.0 M KOH solution was initially examined utilising a two-electrode setup.[31] The comprehensive water splitting efficiency of the catalysts was systematically investigated in 1.0 M KOH electrolyte. Fig. 6a illustrates that, compared with reference samples including $Ni(OH)_2$, Ni_9S_8, Ni_9S_8@N_3Fe-PBA and Ni_9S_8@FeNiP, the Ni_9S_8@Fe-NiP-O_2 catalyst delivered the highest current density at the same cell voltage. At a cell voltage of 2.0 V, the current density of Ni_9S_8@Fe-NiP-O_2 reached 275 mA cm^{-2}, which was far higher than that of $Ni(OH)_2$ (55 mA cm^{-2}). This result verifies that Ni_9S_8@Fe-NiP-O_2 exhibits outstanding bifunctional catalytic activity toward both hydrogen evolution reaction (HER) and oxygen evolution reaction (OER) in alkaline media, thus enabling highly efficient overall water splitting.

The overall water splitting performance was further evaluated in 25% ammonia solution. Fig. 6b illustrates that the Ni_9S_8@Fe-NiP-O_2 catalyst still maintained superior bifunctional activity and outperformed all control samples. When the cell voltage was set at 2.0 V, its current density achieved 210 mA cm^{-2}, remarkably exceeding the 55 mA cm^{-2} of $Ni(OH)_2$. The excellent catalytic performance in ammonia solution confirms its prominent ammonia resistance, endowing it with great application potential in the electrolytic treatment of ammonia-containing wastewater.

The overall water splitting performance of Ni_9S_8@Fe-NiP-O_2 was evaluated in a membrane electrode assembly (MEA) at various temperatures (room temperature, 30 °C, 40 °C, 50 °C, 60 °C) to further examine its practical application potential. Fig. 6c illustrates a significant rise in current density with elevated temperature. At 60 °C, the Ni_9S_8@Fe-NiP-O_2 catalyst attains a current density of 950 mA cm^{-2} at a cell voltage of 2.8 V, significantly surpassing the room temperature value of 610 mA

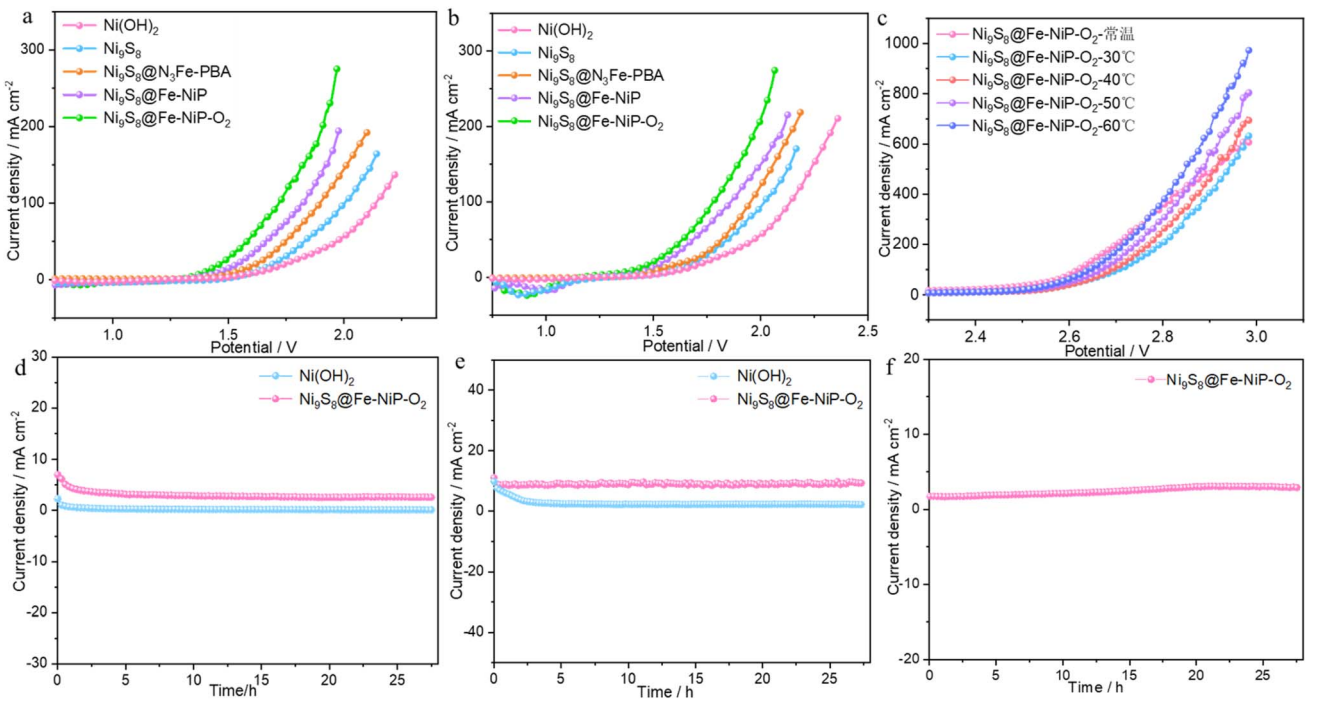


Fig. 6 Overall water splitting performance of the samples (a) LSV curves in 1.0 M KOH solution (b) LSV curves in a 25% ammonia solution (c) LSV curves in a membrane electrode assembly (MEA) (d) constant voltage cycling plot in 1.0 M KOH solution (e) constant voltage cycling plot in a 25% ammonia solution (f) constant voltage cycling plot in a membrane electrode assembly.

© 2026 The Author(s). Published by the Royal Society of Chemistry

cm^{-2}. The superior performance at elevated temperatures is due to expedited reaction kinetics and greater mass transfer rates. The results indicate that the Ni_9S_8@Fe-NiP-O_2 catalyst has significant promise for practical application in industrial-scale water splitting systems.

Fig. 6d–f illustrate the long-term stability assessments of the catalysts. In the 25 hour chronoamperometric tests conducted at a constant potential, the Ni_9S_8@Fe-NiP-O_2 catalyst demonstrated remarkable stability in alkaline electrolyte (Fig. 6d), ammonia-containing electrolyte (Fig. 6e), and the membrane electrode assembly (MEA) system (Fig. 6f), exhibiting no significant decline in current density. This performance significantly exceeds that of the control sample $Ni(OH)_2$, indicating that the catalyst exhibits exceptional structural and performance stability in complicated electrolytes and practical operating circumstances.

3 Conclusion

This study effectively synthesised a bifunctional electrocatalyst featuring a hierarchical core–shell structure (Ni_9S_8@Fe-NiP-O_2). The catalyst has exceptional electrocatalytic performance for both OER and HER in 1 M KOH and 25% ammonia solution, characterised by reduced overpotentials, diminished Tafel slopes, increased electrochemically active surface areas, and markedly enhanced charge-transfer efficiency. Simultaneously, it facilitates efficient comprehensive water splitting in alkaline environments, ammonia solutions, and MEA systems, while providing exceptional large-current density output at 60 °C. The superior catalytic performance arises from the plentiful active sites afforded by the hierarchical porous structure, the optimisation of the reaction energy barrier due to core–shell synergy, and the rapid charge transfer achieved through interfacial electronic regulation.

Conflicts of interest

There are no conflicts to declare.

Data availability

The data that support the findings of this study are available from the corresponding author Depeng Zhao upon reasonable request. Restrictions apply to the availability of these data, which were used under license for the current study. Raw data will be provided after signing a data use agreement to comply with institutional regulations and intellectual property protection requirements.

Supplementary information (SI) is available. See DOI: https://doi.org/10.1039/d6ra04385b.

Acknowledgements

This study was financially supported by the Project of the Education Department of Liaoning Province (LJ212511632006, LJKMZ20221725), College student innovation project (D202604201300000457), Basic Scientific Research Project of Liaoning Provincial Department ofEducation (JYTMS20230305), Liaoning Province Science and Technology Plan Joint Program (2023JH2/101700265, 2023JH2/101700251).

References

1 X. Zou and Y. Zhang, *Chem. Soc. Rev.*, 2015, **44**, 5148–5180.
2 T. Gao, F. Li, S. F. Hung, H. Yang, Y. Sun, K. S. Peng, Q. Sha, Q. Mao, H. Tao, P. Chen and B. Liu, *Nat. Commun.*, 2026, **17**, 1066.
3 T. Li, Y. Zhang, S. Li, H. Zhang, Y. Xu, X. Liu, X. Tian, J. Huang, T. Wang, X. Su, Q. Zhang and Z.-Y. Wu, *ACS Catal.*, 2026, **16**, 8831–8845.
4 X. Wang, P. Yu, M. Liu, L. Wang, F. Shang, F. Zhang, Z. Liu, Y. Bai, K. Liu, L. Zhang, S. Yang, Q. Zhang, T. Cheng and C. Gao, *Nat. Commun.*, 2026, **17**, 1043.
5 T. Wu, S. Zhu, Y. Zhang, X. Lin, L. Liu, H. Ye, H. Wang and Z. J. Xu, *Nat Sustainability*, 2026, **9**, 523–532.
6 H. Yan, N. Zhang and D. Wang, *Chem Catal.*, 2022, **2**, 1594–1623.
7 C. Chen, B. Guo, T. Liu, R. Lin, Y. Liu, Q. Huang, X. Zhang, J. Huang, F. Qian, S. Huang, Q. Chen, X. Mu, S. Mu and Z. Pu, *Chem. Eng. J.*, 2025, **519**, 165088.
8 J. Thakur, P. Phogat and S. Shreya, *Fuel*, 2025, **392**, 134954.
9 S. Li, Y. Xu, X. Zhao, Y. Guo, X. Zhang, C. Zhang, X. Zhang, X. Sun, K. Wang and Y. Ma, *Transactions of Mater. Res.*, 2026, **2**, 100179.
10 T. Yang, S. Han, X. Meng, Y. Dou, D. Yang and J. L. Niu, *J. Am. Chem. Soc.*, 2026, **148**, 18882–18894.
11 H. Wang, H. W. Lee, Y. Deng, Z. Lu, P. C. Hsu, Y. Liu, D. Lin and Y. Cui, *Nat. Commun.*, 2015, **6**, 7261.
12 X. Zhao, P. Pachfule, S. Li, J. R. J. Simke, J. Schmidt and A. Thomas, *Angew. Chem., Int. Ed. Engl.*, 2018, **57**, 8921–8926.
13 S. Anantharaj, S. R. Ede, K. Sakthikumar, K. Karthick, S. Mishra and S. Kundu, *ACS Catal.*, 2016, **6**, 8069–8097.
14 X. Li, X. Hao, A. Abudula and G. Guan, *J. Mater. Chem. A*, 2016, **4**, 11973–12000.
15 X. Ren, L. Qiu, M. Li, F. Tian, L. He, X. Guo, F. Wu, Y. Liu, J. Sheng, W. Yang and Y. Yu, *Appl. Catal., B: Energy Environ. Res.*, 2025, **378**, 125622.
16 Z. Liu, S. Duan, J. Li, Z. Zhao, J. Dai, Y. Zhu, Y. Xu, X. Liu and R. Wang, *Adv. Funct. Mater.*, 2026, e31974.
17 X. Zhang, Y. Wang, C. Liu, Y. Yu, S. Lu and B. Zhang, *Chem. Eng. J.*, 2021, **403**, 126269.
18 P. T. Pham, S. H. Roh, J. Y. Kim and J. K. Kim, *J. Ind. Eng. Chem.*, 2025, **152**, 136–154.
19 L. Du, X. Y. Gao, G. Y. Wang, C. C. Yang and Q. Jiang, *Mater. Res. Lett.*, 2022, **11**, 159–167.
20 D. Acharya, K. Chhetri, I. Pathak, A. Muthurasu, R. Mangal Bhattarai, T. Kim, Y. Raj Rosyara, D. Woo Lee, T. Hoon Ko and H. Yong Kim, *Chem. Eng. J.*, 2024, **499**, 155832.
21 J. Chen, Y. Zhao, S. Zhao, H. Zhang, Y. Long, L. Yang, M. Xi, Z. Ni, Y. Zhou and A. Chen, *Chin. Chem. Lett.*, 2024, **35**, 109268.
22 J. Joo, T. Kim, J. Lee, S. I. Choi and K. Lee, *Adv. Mater.*, 2019, **31**, e1806682.

© 2026 The Author(s). Published by the Royal Society of Chemistry

23 E. Hu, Y. Feng, J. Nai, D. Zhao, Y. Hu and X. W. Lou, *Energy Environ. Sci.*, 2018, **11**, 872–880.
24 Z. Zhao, L. Sui, Z. Wang, S. Song, J. Wang, Y. Li, D. Zhao, G. Li and L. Miao, *Energy Mater.*, 2026, **6**, 600025.
25 C. Han, Z. Ji, Y. Zhu, X. Yao, P. Chen, M. Guo, L. Zhao, X. Lang and Q. Jiang, *Mater. Res. Lett.*, 2022, **10**, 762–770.
26 H. Zhou, S. Xu, B. Zhang, X. Li, Z. Lv, D. Zhao and R.-D. Zhao, *Inorg. Chem. Front.*, 2026, **13**, 666–679.
27 H. Yin, F. Rong and Y. Xie, *Int. J. Hydrogen Energy*, 2024, **52**, 350–375.
28 S. Liu, H. Xuan, Z. Song, L. Meng, J. Wang, X. Liang, Y. Li, Z. Han and P. Han, *Int. J. Hydrogen Energy*, 2024, **59**, 1106–1114.
29 H. Ren, H. Zhou, Q. Zhang, Z. Su, H. Liu, R.-D. Zhao, D. Zhao, Z. Zheng and L. Miao, *J. Colloid Interface Sci.*, 2026, 140606.
30 Y. Feng, L. Huang, Z. Xiao, X. Zhuang, T. S. Aslam, X. Zhang, Y. X. Tan and Y. Wang, *J. Am. Chem. Soc.*, 2024, **146**, 7771–7778.
31 B. Zhang, C. Xiao, S. Xie, J. Liang, X. Chen and Y. Tang, *Chem. Mater.*, 2016, **28**, 6934–6941.

© 2026 The Author(s). Published by the Royal Society of Chemistry